A levitated magnetic dipole configuration as a compact charged particle trap Ⓕ ⓈⒸⒾ

ⒾⒹ H. Saitoh, ⒾⒹ M. R. Stoneking, and ⒾⒹ T. Sunn Pedersen

COLLECTIONS

Ⓕ   This paper was selected as Featured

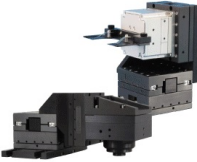ⓈⒸⒾ   This paper was selected as Scilight
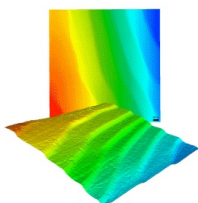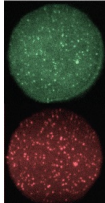
🌐 **View Online**   ⬆ **Export Citation**   Ⓡ **CrossMark**

ARTICLES YOU MAY BE INTERESTED IN

91, 043507

A levitated magnetic dipole configuration as a compact charged particle trap ⓕ ⓢⓒⓘ

View Online Export Citation CrossMark

H. Saitoh,[1,2,a)] ⓘⒹ M. R. Stoneking,[2,3] ⓘⒹ and T. Sunn Pedersen[2,4] ⓘⒹ

AFFILIATIONS

[1] Graduate School of Frontier Sciences, The University of Tokyo, Kashiwa, Chiba 277-8561, Japan
[2] Division E4, Max Planck Institute for Plasma Physics, Greifswald 17491 and Garching 85748, Germany
[3] Department of Physics, Lawrence University, Appleton, Wisconsin 54911, USA
[4] Institute of Physics, The University of Greifswald, Greifswald 17489, Germany

[a)] Author to whom correspondence should be addressed: saito@ppl.k.u-tokyo.ac.jp

ABSTRACT

As a magnetic confinement configuration for electron–positron pair-plasmas, the APEX collaboration [T. S. Pedersen *et al.*, New J. Phys. **14**, 035010 (2012)] plans to construct a compact levitated dipole experiment with a high-temperature superconducting coil. In order to realize stable levitation of the dipole field coil, a simple feedback-controlled levitation system was constructed with conventional analog circuits. We report the properties of a prototype levitation system using a permanent magnet and compare its behavior to predictions from a stability analysis. We also present a practical review needed for the construction of a compact levitated dipole trap system based on the work of Morikawa *et al.* [Teion Kogaku, J. Cryo. Soc. Jpn. **39**, 209 (2004)]. Numerical orbit analysis suggests improved confinement properties of charged particles in a dipole field trap by replacing the permanent magnet with a levitated superconducting coil magnet. Such a compact dipole field configuration is potentially applicable to the confinement of various charged particles including positrons and electrons.

Published under license by AIP Publishing. https://doi.org/10.1063/1.5142863

I. INTRODUCTION

After studies of plasma confinement in internal conductor devices in the 1970s,[1] experiments in a levitated dipole configuration, or *a laboratory magnetosphere*,[2] are being carried out that focus on the relaxation states of plasmas suitable for advanced fusion concepts. The Ring Trap (RT) project of The University of Tokyo was motivated by efficient plasma confinement observed in the Jovian magnetosphere,[3] which is explained by the theory of self-organization of flowing plasmas.[4,5] The basic concept of dipole confinement was investigated in Proto-RT,[6,7] where the dipole field was generated by a mechanically supported copper coil. In order to minimize perturbations to plasmas caused by the mechanical support structures of the coil, a levitated high-temperature superconducting coil was developed and used in the Mini-RT experiment.[8] Based on these basic studies, RT-1 was constructed and started operation in 2006.[2] In RT-1, physics of both fusion-oriented high temperature plasmas and non-neutral plasmas has been investigated.[9,10] Another approach to the advanced fusion concept in the dipole

field configuration[11] has also been studied at the Levitated Dipole Experiment (LDX)[12] whose levitation system design is reported in Ref. 13.

As a confinement geometry for non-neutral plasmas[14] including antimatter plasmas[15] and other charged particles,[16–19] toroidal geometries may be attractive because of their capability to confine charged particles consisting of multiple species at any non-neutrality.[20,21] In the axisymmetric magnetic configuration of the dipole, excellent charged particle confinement properties are expected because of the conservation of the canonical angular momentum. By utilizing this property, the A Positron–Electron eXperiment (APEX) collaboration plans to use a compact levitated dipole geometry as the magnetic trapping configurations for electron–positron pair-plasmas. Experimental understanding of the unique properties of the pair-plasmas[22,23] is the final goal of APEX. Another approach to an electron–positron plasma creation is also underway using an intense laser.[24,25] Initial experiments with a mechanically supported permanent magnet,[26] operated at the NEutron induced POsitron Source MUniCh (NEPOMUC) positron

facility,[27] achieved loss-less injection of the positron beam into the closed dipole field configuration[28] and stable trapping of positrons.[29] These experiments with the low energy positron beams of NEPO-MUC[30,31] demonstrated the excellent confinement properties of the dipole magnetic field configuration.

One of the next major milestones of the APEX project is the simultaneous confinement of both positrons and electrons in the dipole field configuration. For the stable confinement of pair-plasmas, the levitation of a dipole field coil magnet is needed, which may be realized by using a feedback-controlled levitation system. In addition to its application for the realization of electron–positron plasmas, using low-energy positrons or using intense lasers, this configuration is also potentially applicable for trapping multiple charged particle species for ion and plasma physics experiments.

In this study, we developed a feedback-controlled magnetic levitation system to be used for the compact levitated dipole experiment of the APEX project. Although Earnshaw's theorem[32] forbids stable levitation of an object against gravity with static electric and magnetic fields, there are several methods to stabilize the levitation.[33–38] In Sec. II, we review the mechanism of magnetic levitation with a feedback-controlled system[39–43] and consider the practical choice of the operation parameters of the levitation system for a charged particle trap. In Sec. III, we report on a simple feedback-controlled levitation system realized using conventional analog circuits[44] and analyze the stability of the system. The properties of the magnetic levitation with this system are investigated using a small permanent magnet and compared with the stability analysis. In Sec. IV, we analyze the orbit of charged particles in a compact levitated dipole experiment in comparison with a permanent magnet dipole field configuration.

II. EQUILIBRIUM AND STABILITY ANALYSIS OF MAGNETIC LEVITATION

A. Force balance for a floating magnet

In this section, we review the levitation mechanism needed for the stability analysis and levitation experiments.[41,43] Figure 1 shows a typical geometry of a magnetic levitation experiment. We assume that a circular floating (F) coil or a magnet is levitated at the equator ($z = 0$) of the experiment using an upward magnetic force from a circular levitation (L) coil. We anticipate coaxially placing the L coil above the F coil to provide an upward levitation force if the currents are in the same direction. In addition, we choose a configuration to stabilize the tilt motion of the F coil, as we will discuss later. According to the vertical position of the F coil, which is monitored by using a laser positioning sensor, for example, the L coil current is adjusted with a feedback-controlled system. The L coil carries a total current of $I_L N_L$, which generates an attractive magnetic force to levitate the F coil with a mass m_F and a total current of $I_F N_F$. Here, I_L and I_F are coil currents, and N_L and N_F are the numbers of turns in each coil. The major radius and the vertical position of the F coil are r_F and z_F, respectively. Although we perform this analysis with the levitation of a superconducting coil in mind, we take the current in the F coil to be fixed in the following analysis. While magnetic flux is conserved for a superconductor, we can choose a levitation configuration so that the expected variation in the current associated with the perturbations we consider is negligible.
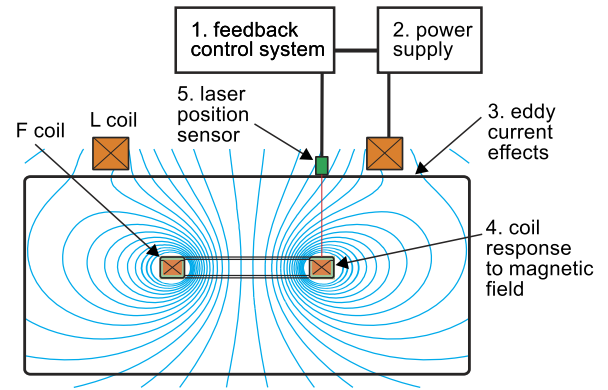

FIG. 1. A schematic of a typical levitated dipole experiment and its feedback-controlled levitation system.

The vertical motion of the F coil in this system is determined by the equation of motion,

$$m_F \frac{d^2 z_F}{dt^2} = -2\pi r_F N_F I_F B_r - m_F g, \tag{1}$$

where B_r is the radial component of magnetic field at the location of the F coil (r_F, z_F) generated by the L coil. Here, the current in both coils is taken to be in the positive azimuthal direction (counterclockwise when viewed from above). For a ring current, the radial component of the field may be numerically calculated using complete elliptic integrals of the first and second kinds, $K(k)$ and $E(k)$. We assume that the circular L coil of radius r_L, current I_L, and N_L turns is located at the vertical position of $z = z_L$. By using $K(k)$ and $E(k)$, where

$$k = \sqrt{\frac{4 r r_L}{(r + r_L)^2 + (z - z_L)^2}}, \tag{2}$$

the radial component of the magnetic field generated by the L coil at (r, z) is

$$B_r(r, z) = \frac{\mu_0 N_L I_L (z - z_L)}{2\pi r ((r + r_L)^2 + (z - z_L)^2)^{1/2}}$$
$$\times \left(-K(k) + \frac{r_L^2 + r^2 + (z - z_L)^2}{(r_L - r)^2 + (z - z_L)^2} E(k) \right). \tag{3}$$

Because B_r is proportional to the L coil current I_L for a fixed geometry and fixed N_L, we may write (1) as

$$m_F \frac{d^2 z_F}{dt^2} = -2\pi r_F N_F h I_F I_L - m_F g \tag{4}$$

using

$$B_r(r_F, z_F) = h(r_F, z_F) I_L. \tag{5}$$

In the equilibrium state of (4), the force balance equation is

$$2\pi r_F N_F h I_F I_L + m_F g = 0. \tag{6}$$

For a fixed geometry of the F coil, the upward force on the L coil is proportional to B_r generated by the F coil. This field strength profile is explained in Subsection II B.

B. Stability of levitation

In order to evaluate the stability of the vertical coil motion, we define the inverse scale length, α, for the change in the vertical magnetic force $F_z(z)$ as

$$\alpha(z) = \frac{dF_z/dz}{F_z} = \frac{d(I_F B_r)/dz}{I_F B_r}. \tag{7}$$

The vertical coil motion is unstable when α is positive. For a permanent magnet, (7) becomes

$$\alpha(z) = \frac{1}{B_r}\frac{dB_r}{dz} = \frac{1}{h}\frac{dh}{dz}, \tag{8}$$

assuming that the field of the magnet is generated by an equivalent ring current.

The typical oscillation frequency of the F coil is an important system parameter toward the development of a feedback-controlled stabilizing system. For the small vertical oscillation motion of the F coil near the equilibrium point of $z = 0$, the coil oscillation motion is approximated as a harmonic oscillation in a restoring force of

$$F_z(z) = -kz = -2\pi r_F I_F N_F \frac{dB_r}{dz} z. \tag{9}$$

The vertical oscillation frequency of the F coil is then

$$f = \frac{1}{2\pi}\sqrt{\frac{2\pi r_F I_F N_F}{m_F}\frac{dB_r}{dz}}. \tag{10}$$

For the parameters of a permanent magnet levitation system described below, we have $f = 5$ Hz. In general, it is difficult to stabilize fast oscillations using a feedback-controlled system. This is mainly because of the effects of delay times of the system, caused by the finite response speed of a power supply and laser positioning sensor, and eddy currents. Thus, stabilization of the slower vertical motion of a larger-mass coil is easier although the entire properties of the levitation system of course depend on many parameters in addition to the characteristic frequency.

The motions of a floating coil magnet are classified into vertical, slide, and tilt motions, as shown in Fig. 2. We review the linear stability analysis of these motions with respect to the position of the F

and L coils, in order to decide the operation parameters of the experiment. Variation of the magnetic force on a small coil segment due to a vertical displacement is given by

$$\frac{d(N_F I_F B_r)}{dz} = N_F I_F \frac{dB_r}{dz}, \tag{11}$$

again assuming that I_F is constant.

For the vertical motion shown in Fig. 2(a), we consider the Lorentz force working at one point of the F coil because of the axial symmetry of the system. With a small vertical deviation Δz of the coil position from the equilibrium point of $z = 0$, the radial magnetic field at the F coil position at $r = r_F$ is

$$B_{r1} = B_{r0} + \left.\frac{\partial B_r}{\partial z}\right|_{r=r_F, z=0}\Delta z, \tag{12}$$

where B_{r0} is a value at the equilibrium point. This vertical motion is stable when

$$0 < \left.\frac{\partial B_r}{\partial z}\right|_{r=r_F, z=0}, \tag{13}$$

generating a restoring force for a positive deviation of Δz. Because B_r is generally negative in the assumed configuration, this condition means that the absolute value of B_r is a decreasing function of z near $z = 0$.

For the slide instability, we consider the Lorentz forces working at two symmetric points on the F coil, as shown in Fig. 2(b), again due to the symmetry of the system. With a small position deviation Δr in a horizontal direction, the vertical magnetic field strengths at the two positions are

$$B_{z1} = B_{z0} + \left.\frac{\partial B_z}{\partial r}\right|_{r=r_F, z=0}\Delta r, \tag{14}$$

$$B_{z2} = B_{z0} - \left.\frac{\partial B_z}{\partial r}\right|_{r=r_F, z=0}\Delta r \tag{15}$$

Because the F coil current is the same at positions 1 and 2, the stability condition is simply

$$B_{z1} < B_{z2}. \tag{16}$$

From (14) and (15), the slide motion is stable when

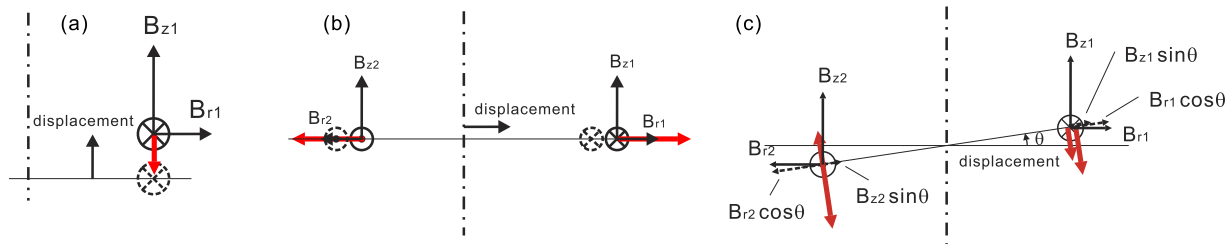$$\left.\frac{\partial B_z}{\partial r}\right|_{r=r_F, z=0} < 0. \tag{17}$$

FIG. 2. When the magnetic field components are positive in the directions shown (black arrows) and the direction of the current is indicated (counterclockwise from above), the forces on the coil to decide stabilities (red arrows) are shown for (a) vertical, (b) slide, and (c) tilt displacements of the F coil from the equilibrium levitation position.
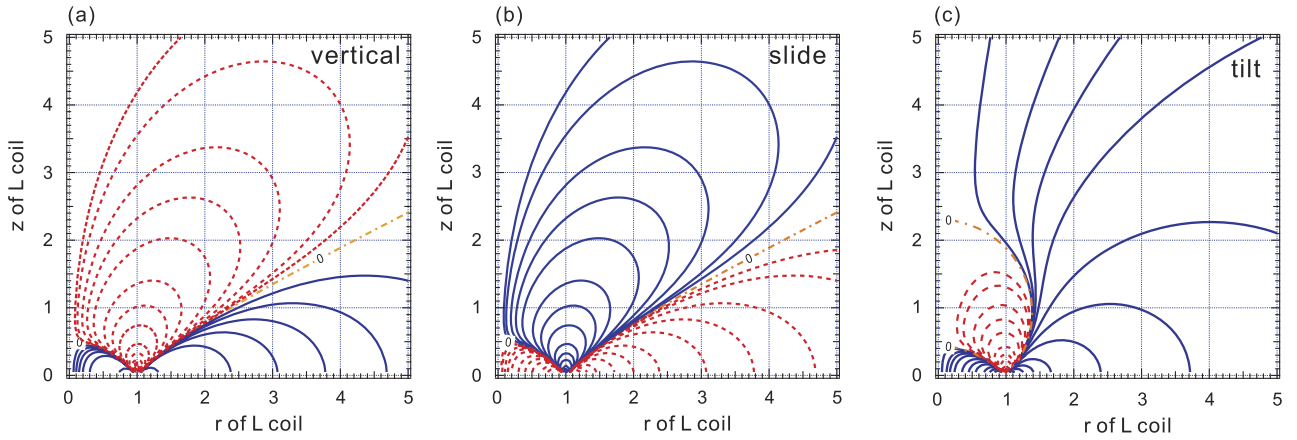
FIG. 3. Stability maps of the (a) vertical, (b) slide, and (c) tilt motions of the F coil as functions of the radius and vertical position of the L coil. The radius and vertical position of the F coil are normalized to be $r = 1$ and $z = 0$, respectively. Regions satisfying conditions (13), (17), and (23) are plotted as blue solid lines, while red dashed lines show unstable regions. The chain lines in orange labeled "0" are the stability boundaries.

For the tilt motion of the F coil, as shown in Fig. 2(c), we consider a small angular deviation from the equilibrium position and compare the Lorentz forces working at two symmetric points of the F coil. There are four force components that produce torque on the coil. They depend on the following quantities using the small angle approximation:

$$B_{r1} \cos\theta \sim B_{r0} + \left.\frac{\partial B_r}{\partial z}\right|_{r=r_F, z=0} r_F\theta, \tag{18}$$

$$B_{z1} \sin\theta \sim B_{z0}\theta, \tag{19}$$

$$B_{z2} \sin\theta \sim B_{z0}\theta, \tag{20}$$

$$B_{r2} \cos\theta \sim B_{r0} - \left.\frac{\partial B_r}{\partial z}\right|_{r=r_F, z=0} r_F\theta. \tag{21}$$

The tilt motion is stabilized when

$$B_{r2}\cos\theta < B_{r1}\cos\theta + B_{z1}\sin\theta + B_{z2}\sin\theta, \tag{22}$$

which yields

$$0 < B_{z0} + r_F \left.\frac{\partial B_r}{\partial z}\right|_{r=r_F, z=0}. \tag{23}$$

These stability conditions solely depend on the spatial configuration of the F and L coils. We plot (13), (17), and (23) in Fig. 3 for various L coil positions by fixing the position of the F coil at a normalized position. Specifically, we assume that the F coil is approximated as a ring current with a radius of $r = 1$ and located on the $z = 0$ plane. The contours with dashed lines show the unstable regions, while regions with solid lines satisfy the stable conditions. A clear interpretation from the diagrams is that it is impossible to stabilize all these instabilities simultaneously just by adjusting coil configuration. This can be understood because, in a current-free region where the curl of the magnetic field is zero, the RHS of (13) equals the LHS of (17). Therefore, vertical and slide motions are not simultaneously

stabilized, as shown in Figs. 3(a) and 3(b). Vertical instability is one-dimensional, while slide instability is two-dimensional. Because the detection and control of one-dimensional motions are much easier than those for two-dimensional displacements, we chose a coil configuration so that the F coil is stable for the slide motion and unstable for the vertical motion. The remaining vertical instability may be stabilized by using a feedback-controlled system, as explained in Sec. III. As shown in Fig. 2(c), the tilt motion can be stabilized by

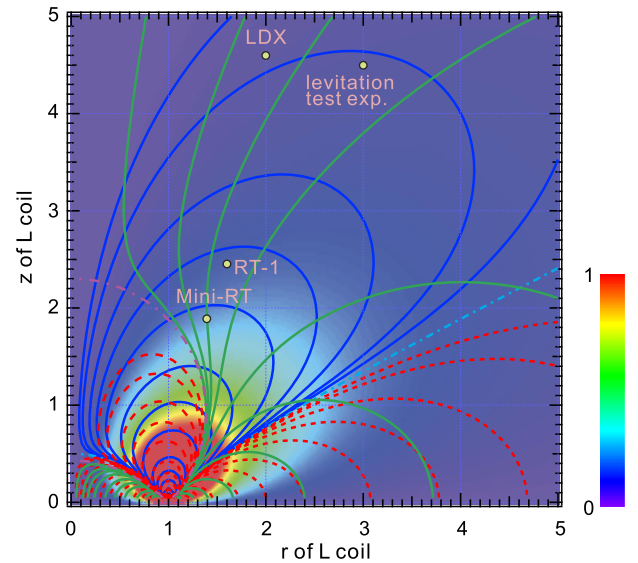**FIG. 4**. Color contours show the radial magnetic field B_r at the F coil position of $(r, z) = (1, 0)$ generated by the L coil located at various positions. The field strength is normalized to the value at $(r, z) = (1, 0.5)$. Lines show stable (solid lines) and unstable (dashed lines) regions for slide and tilt motions of the F coil for various L coil positions and the F coil fixed at $(r, z) = (1, 0)$.

placing the L coil at a location to avoid instability. In particular, if the L coil radius is more than 1.4 times the radius of the F coil, the tilt stability is assured. It is known that the tilt instability may be stabilized by using additional coils, but we will focus on a two-coil system in this study.

In addition to the stability conditions, we need to consider the levitation force required to realize the efficient levitation of the coil magnet, which is related to the required capacity of the L coil and power supplies. This is determined by the magnitude of the radial magnetic field generated by the L coil at the position of the F coil. The color contours in Fig. 4 plot B_r generated by the L coil at the position of the F coil as a function of the L coil position. The stabilities of slide and tilt motions are also superimposed in Fig. 4. From the color contours of field strength, one can see that for a given L coil radius, there can be two vertical-equilibrium positions to realize the levitation of the F coil. One of these L coil positions is always in the region of slide stable (vertical instability) and the other is slide unstable (vertically stable). The coil configuration may be decided according to these equilibrium and stability properties of the levitation system. Parameters of the several levitated dipole experiments and a levitation test experiment, to be described in Sec. III, are also plotted in Fig. 4. All the experiments shown are stable for slide and tilt motions but unstable for the vertical motion.

III. LEVITATION SYSTEM AND STABILITY ANALYSIS

Through the analysis summarized in Sec. II B, it is clear that a feedback-controlled system is required to stabilize the vertical motion of the F coil. In this section, we construct such a system using conventional analog circuits with a test levitation experiment using a permanent magnet. The stability of the system is analyzed using transfer functions,[43] and the analysis is compared with experimental results.

A. Levitation analysis and test experiment

Figure 5 shows the flow chart of the levitation system corresponding to Fig. 1.[43] The position signal from a laser sensor is sent to a feedback-control circuit that produces an output signal accordingly. This output signal controls the current of the L coil so that the F coil is stably levitated. In a real experiment, there is a time lag between the L coil current and B_r at the F coil because of the eddy currents induced in conductors (e.g., a vacuum chamber). The F coil responds to B_r according to the equation of motion.

We investigated levitation stabilization using a simple experiment with a permanent magnet, as shown in Fig. 6. A cylindrical
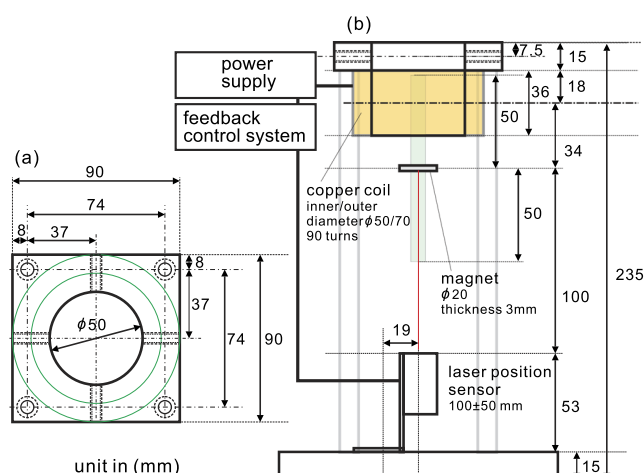

FIG. 6. A schematic of a levitation test experiment with a permanent magnet: (a) the top view and (b) the side view of the experiment. The magnet is stably levitated by the magnetic force of a levitation coil whose current is feedback-controlled according to the magnet position.

neodymium magnet (MISUMI HXN20-3) of diameter 20 mm, height 3 mm, and weight 7 g was levitated with this system. Including buffer material wrapped around the magnet, the total weight of the magnet was 8.4 g. Field strength at the magnet surface was 0.18 T, according to a measurement with a Hall magnetic sensor probe. The magnetic field of this permanent magnet is approximated as a current loop of 2990 A and a diameter of 20 mm. The levitation coil with 90 turns was located above the magnet, as shown in Fig. 6, and was operated at a current of 7 A for the equilibrium levitation point of the magnet at $z = 0$ cm. The levitation coil was approximated as a current loop of 630 A and a diameter of 60 mm. The levitation coil current was supplied by a 10 A power supply, Elektro-Automatik PS3065-10B, whose output current was externally controlled by input voltage into its analog interface. The vertical magnet position was monitored by a laser sensor, Sick OD-1, which can measure a distance in a range of 50 and 150 mm from the sensor head. This laser sensor had an analog voltage output between 0 V and 10 V proportional to the object's position in the measurable range.

We use a proportional-integral-derivative (PID) circuit to provide feedback to the L coil power supply which is made with easily available and low cost analog operational amplifiers, as shown in Fig. 7. This circuit is based on the design of Morikawa.[39] We used Analog Devices OP97, low-noise small-drift operational amplifiers. At present, this is a circuit that used one laser position sensor system with only one input interface. The analog output signal from a laser position sensor is sent to U1 and U2. In future experiments, we plan to add two laser sensors, using U2 as an averaging circuit for the three inputs. The output signal from U2 is sent to a differential amplifier U3. The output voltage from U3 is proportional to the difference between the coil position signal and a reference signal V_{ref}. This signal $V_{err} = V_i - V_{ref}$ is called an error signal. Here, V_{ref} was generated by using an adjustable voltage regulator, Texas Instruments LM317. The output of the differential amplifier U3 is
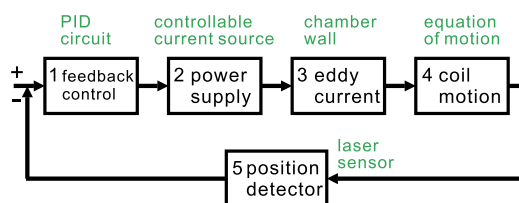

FIG. 5. Flow chart for the levitation system of a levitated dipole experiment.
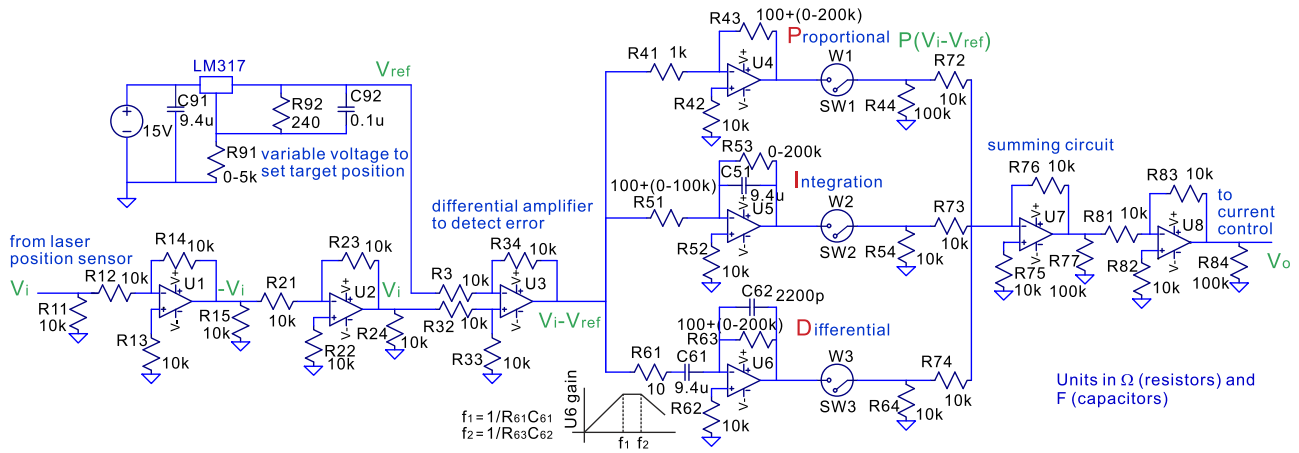
FIG. 7. A PID control system realized by conventional analog components to feedback-control the L coil current for the F coil and magnet levitation using the signal from a laser positioning sensor. U1-8 are Analog Devices OP97 with 0.1 μF bypass capacitors at each power supply pins. DC voltages of ± 15 V were supplied by a series-regulated power supply.

then sent to the P, I, and D circuits, which generates

$$V_P = -\frac{R_{43}}{R_{41}} V_{err}, \qquad (24)$$

$$V_I = -\frac{1}{R_{51}C_{51}} \int V_{err} dt, \text{ and} \qquad (25)$$

$$V_D = -R_{63}C_{61} \frac{dV_{err}}{dt}. \qquad (26)$$

These signals were combined by a summing circuit U7. The output voltage of inverter U8, V_O, was used as a current control signal, which was sent to the control interface of the power supply of the L coil.

In order to stabilize the D component of the circuit, around U6 in Fig. 7, the bandwidth of this amplifier was limited with the characteristic frequencies of $f_1 = 1/R_{61}C_{61}$ and $f_2 = 1/R_{63}C_{62}$, as shown in Fig. 7, which should be much higher than the oscillation frequency of the F coil motion. In deciding the value of f_2, it should also be considered that R_{63} is a variable resistance. One should also try to reduce the capacitive component between the output of U6 and the ground in constructing the circuit. When the transfer length between the laser positioning system and the PID control circuit was long, we found that a conventional RC low pass filter with a time constant of ~1 ms, installed at the input of the PID circuit, was efficient in reducing the noise in the position signal. In order to avoid the switching noises, DC voltages for the circuits were supplied by a series regulator based power supply circuit.

The transfer function of each component of the PID circuit is related to the total circuit transfer function G_1 by

$$G_1 = P + Ds + I\frac{1}{s} \sim P\left(1 + \frac{D}{P}s\right), \qquad (27)$$

where $s = j\omega$, $P = R_{43}/R_{41} < 200$, and $D = R_{63}C_{61} < 1.88$ with parameters in Fig. 7. Here, we neglect the I component, which is not necessarily needed for levitation and often satisfies $I/s \ll P, Ds$.

The time responses of the system with the L coil and its power supply are shown in Fig. 8(a). For the L coil power supply system, we approximate G_2 as

$$G_2 = \gamma \frac{1}{1 + s/909} \quad (A/V), \qquad (28)$$

a first-order transfer function with a 1.1 ms time constant, which was obtained by an exponential fitting as shown in the figure. Here, γ is the gain of the power supply, i.e., output current (A) per input voltage (V), and $\gamma = 1$ in this experiment.

Eddy current effects increase the response time of the system, which also may be approximated as a first-order transfer function. However, because the test experiment has no vacuum chamber, we ignore the eddy current effects as

$$G_3 = 1. \qquad (29)$$

The equation of motion of the F coil is linearized by taking $I_L = I_{L0}(1 + I_d/I_{L0})$ and $h = h_0(1 + \alpha z)$ as

$$m_F \frac{d^2z}{dt^2} = -2\pi r_F N_F h_0 I_F I_{L0}\left(1 + \frac{I_d}{I_{L0}} + \alpha z\right) - m_F g. \qquad (30)$$

Because the equilibrium requires $-2\pi r_F N_F h_0 I_F I_{L0} - m_F g = 0$, we have

$$m_F \frac{d^2z}{dt^2} = m_F g\left(\frac{I_d}{I_{L0}} + \alpha z\right). \qquad (31)$$

By taking the Laplace transform, this equation becomes

$$s^2 Z(s) = \frac{g}{I_{L0}} I_d(s) + g\alpha Z(s). \qquad (32)$$

Then, the transfer function of the coil motion is

$$G_4 = \frac{Z(s)}{I_d(s)} = \frac{1}{I_{L0}\alpha} \frac{1}{s^2/(g\alpha) - 1}. \qquad (33)$$
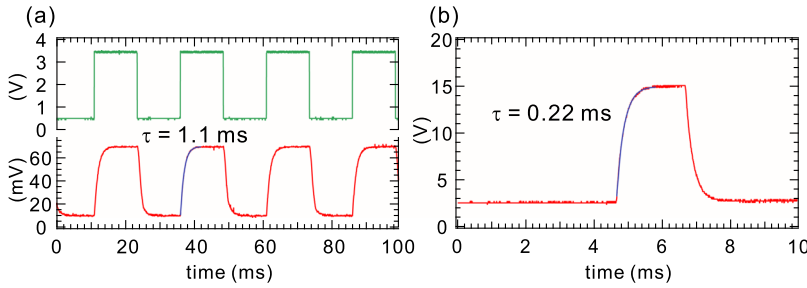
FIG. 8. (a) Time response of a system with the L coil and power supply PS3065-10B, current output signal (bottom) against the input of rectangular control voltage (top). (b) Time response of laser position sensor OD-1, against fast (<0.1 ms) change in a target position.

For the present parameters, the force balance is realized when the L coil, approximated by a ring current, is located at $z = 4.75$ cm. We numerically calculate B_r, dB_r/dz, and α, as shown in Fig. 9. Because $B_r = 0.436$ mT and $dB/dr = -0.0234$ T/m at $z = 0$ cm, at the position of the F coil, we have $\alpha = 54.1$/m. The L coil current was $I_{L0} = 7$ A. For these parameters, the transfer function of the equation of motion is given by

$$G_4 = \frac{1}{379}\frac{1}{s^2/530 - 1} \quad \text{(m/A)}. \tag{34}$$

Because the variation of α and B_r is relatively weak near the equilibrium point, as shown in Fig. 9, it is expected that the stability condition is also not very sensitive around $z = 0$. This suggests the possibility of stable magnetic lift up and landing of the magnet by controlling the levitation coil current.

For the laser sensor, whose time responses are shown in Fig. 8 (b), we include the response time of 0.22 ms for the first-order transfer function and a gain of 100, which yields

$$G_5 = 100\frac{1}{1 + s/4550} \quad \text{(V/m)}. \tag{35}$$

By combining G_1 to G_5 using the block diagram in Fig. 5, we have the total transfer function $G_T = G_1G_2G_3G_4/(1 + G_1G_2G_3G_4G_5)$ which can be written as

$$G_T = \frac{\frac{P}{379}\left(1 + \frac{D}{P}s\right)\left(1 + \frac{s}{4550}\right)}{\left(1 + \frac{s}{909}\right)\left(\frac{s^2}{530} - 1\right)\left(1 + \frac{s}{4550}\right) + \frac{100}{379}P\left(1 + \frac{D}{P}s\right)} \tag{36}$$

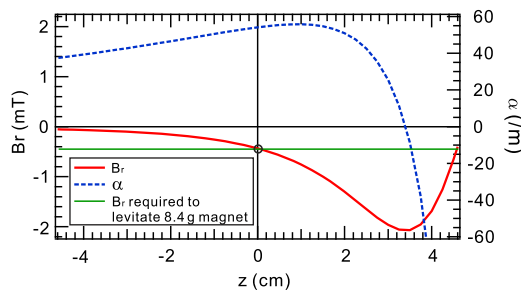for the entire levitation system. The characteristics equation of the system is written as, by using the characteristic polynomial, the denominator of this equation,

$$a_4s^4 + a_3s^3 + a_2s^2 + a_1s + a_0 = 0, \tag{37}$$

where $a_4 = 4.56 \times 10^{-10}$, $a_3 = 2.49 \times 10^{-6}$, $a_2 = 1.89 \times 10^{-3}$, $a_1 = 0.264D - 1.32 \times 10^{-3}$, and $a_0 = 0.264P - 1.00$. The solutions of the characteristic equation are called poles. In order that the system is stable, the real parts of all poles must be negative. Otherwise, i.e., when the characteristic equation has a positive pole, the step response (the response of a system for the input of a step function) has a divergent exponential term. Here, in order to determine the stability of this system, we use the Routh–Hurwitz stability criterion,[45] which is equivalent to the above statement about the poles. According to this criterion, the stability conditions of this system are the following three equations:

$$a_n > 0, \tag{38}$$

$$\begin{vmatrix} a_3 & a_1 \\ a_4 & a_2 \end{vmatrix} = a_3a_2 - a_4a_1 > 0, \quad \text{and} \tag{39}$$

$$\begin{vmatrix} a_3 & a_1 & 0 \\ a_4 & a_2 & a_0 \\ 0 & a_3 & a_1 \end{vmatrix} = a_3a_2a_1 - a_4a_1^2 - a_3^2a_0 > 0. \tag{40}$$

From these equations, we have the stability conditions of the system as follows:

$$5.00 \times 10^{-3} < D < 39.0, \quad \text{and} \tag{41}$$

FIG. 9. The values of B_r and α of the levitation test experiment for different vertical positions of the magnet. The L coil is located at $z = +4.75$ cm.
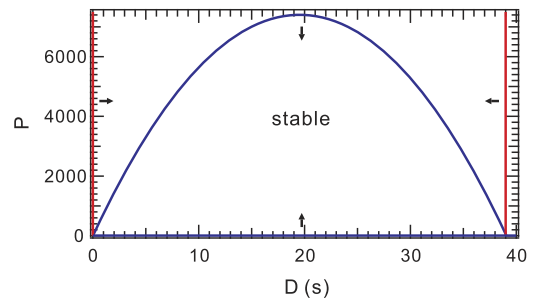

FIG. 10. Stability conditions in (41) (red lines) and in (42) (blue lines) of the levitation test experiment for various D and P values. The arrows indicate conditions to satisfy these equations.

$$3.79 < P < -19.4D^2 + 758D. \tag{42}$$

Lines in Fig. 10 show these conditions. The vertical motion of the F coil is stabilized by choosing appropriate feedback parameters. Experimentally, it is convenient to operate in the lower left region of stability where the values of P and D are simultaneously smaller.

B. Levitation experiments

By using the system described above, we tested the feedback-controlled levitation of a permanent magnet. The magnet was initially placed below the equilibrium point on a supporting plate at $z = -1.3$ cm, and smoothly moved up to $z = 0$ cm by adjusting V_{ref} of the control circuit. As shown in Fig. 11, the magnet was stably levitated without time constraints when the V_{ref}, P, and D values were appropriately adjusted. At the end of the levitation, the magnet was moved down to $z = -1.3$ cm again by adjusting the value of V_{ref}.

The equilibrium levitation state is realized as follows: For a fixed equilibrium coil position, the L coil current I_{L1} and the position signal V_{i1} from a laser sensor are fixed values. This equilibrium is decided according to the equation of motion in the gravity. Here, two conditions pertain (1) that the L coil current is sufficient to satisfy the minimum equilibrium requirements for the F coil (magnet) parameters and (2) that the values of P and D satisfy (41) and (42). The DC component of the output from the feedback circuit is $V_O = -P(V_{i1} - V_{ref})$. The DC coil current may be controlled so that it is proportional to V_O, and we can write it as $-\gamma P(V_{i1} - V_{ref})$. Then, this system has a steady state solution determined by the control variables V_{ref} and P so that

$$I_{L1} = -\gamma P(V_{i1} - V_{ref}) \tag{43}$$

is satisfied. The F coil is levitated at a certain point according to the values of V_{ref} and P. According to the velocity of the levitated magnet, the D component of the circuit provides a stabilization force on the magnet. It is noted that we can realize an equilibrium solution with a same I_L value and the vertical position with various sets of V_{ref} and P values. We confirmed this relation in (43) with experiments. In the present experimental setup, we have $\gamma = 1$. In Fig. 12, we plot values of V_{ref} and P for the constant L coil current of $I_L = 7$ A and a constant magnet position of $z = 0$ cm, which showed good agreement with (43).

FIG. 12. Set of V_{ref} and P values that realized stable levitation of the magnet at $z = 0$ cm (circles) and the plot of (43), where $\beta = 1$ (solid line).

Finally, we compare the levitation condition with the stability analysis. Circles in Fig. 13 show minimum D values needed for stable levitation for various P values. We found that levitation was realized when $6.6 \times 10^{-3} \leq D$ and $4.1 \leq P$. When P was below this value, the magnet was not levitated stably with any D value. These values showed fairly good agreement with (41) and (42), in spite of the use of a rather simplified analysis model. When the P and D values were close to the stability condition lines in Fig. 13, the magnet behavior was irregular. The magnet position was often stable for a very short time, but eventually the vertical instability grew, which was sometimes stabilized for another short time and sometimes not. Such a non-reproductive behavior might be caused by magnetic field errors and the rotation of the magnet with small structural and field asymmetries, as well as by the effects of electromagnetic noise in the experiment environment. As criteria for determination of stability in this figure, we judged that the system is stable when the magnet was levitated for more than 10 s without significant fluctuations. When the D value was typically two times larger than the critical value expected by (42), the magnet was stably levitated without time constraints, as shown in Fig. 11.
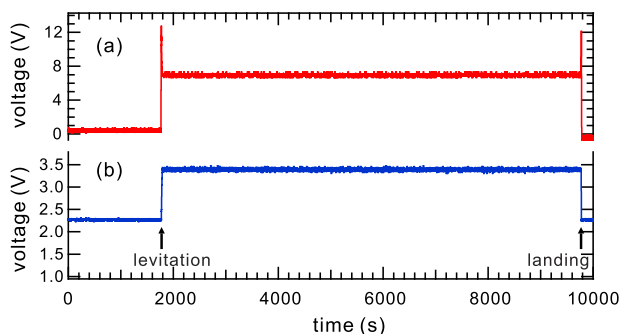

FIG. 11. Long time (~ 8000 s) levitation of the permanent magnet realized by the stabilization of its vertical motion by the feedback-controlled system. Signals of (a) the laser sensor position output and (b) the PID control circuit output.
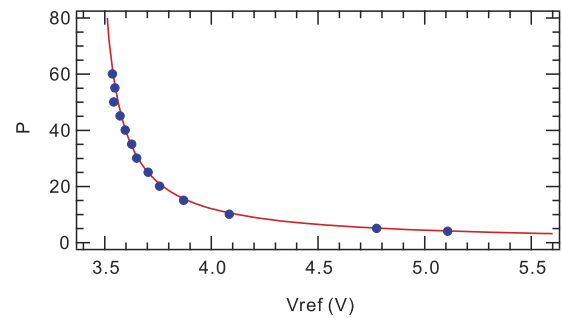

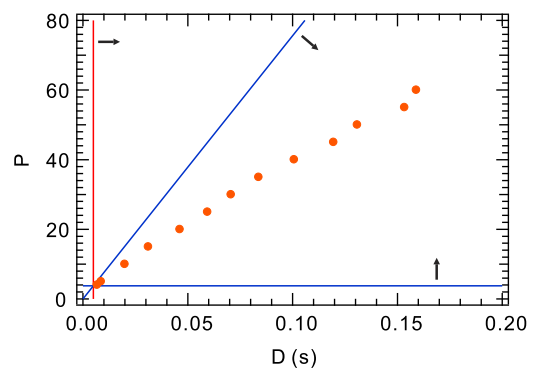**FIG. 13**. Comparison of the levitation experiment and stability conditions. Minimum values of D required for the stable levitation (see main text) are plotted as circles for different P values. Numerically obtained stability conditions of (41) (red line) and (42) (blue lines) are also plotted (the arrows indicate conditions to satisfy these equations) for comparison around the measurement region (near the origin of Fig. 10).

IV. TRAPPING PROPERTIES IN PERMANENT MAGNET AND LEVITATED DIPOLE GEOMETRIES

As demonstrated in the prototype APEX experiment at the NEPOMUC slow positron facility,[29] in a dipole magnetic field configuration generated by a permanent magnet, charged particles including positrons are confined for a fairly long time. Because the field lines of a permanent magnet intersect the magnet surface, as shown in Fig. 14(a-1), the upper limit of the trapping time may be set by recombination loss at the magnet surface caused by the collisional transport of particles into the loss cone of the magnetic mirror. In real experiments, it is not straightforward to predict the trapping properties of a dipole field trap because of various parameters, including the injection conditions, vacuum, and remaining gas species, and the electric and magnetic symmetry of the system in relation to the conservation of canonical angular momentum. In the prototype APEX experiment with a moderate vacuum condition, it was found that the loss cone effects caused by collisions with

neutral molecules were an important loss channel of positrons.[29] For single-component non-neutral plasmas, such a loss channel on the magnet surface may be suppressed by applying a DC voltage on the magnet so that trapping electric fields are generated. However, when the trap is asymmetric, for example, because of its injection $\mathbf{E} \times \mathbf{B}$ plates located near the trapping region of the APEX experiment,[28] bias voltage on the magnet generates asymmetric electric fields that break the conservation of canonical angular momentum of a trapped particle. This can cause a significant degradation of the confinement properties of the trap. Furthermore, when we try to confine multi-component plasmas including electrons and positrons, we cannot apply such bias voltage on the magnet in order to avoid the mirror loss of both of particles.

The particle decay caused by the transport of particles into the loss cone is reduced by replacing the permanent magnet with a levitated superconducting (SC) ring coil in the trap, as shown in Fig. 14, which is planned to be used in the APEX experiment. In contrast to
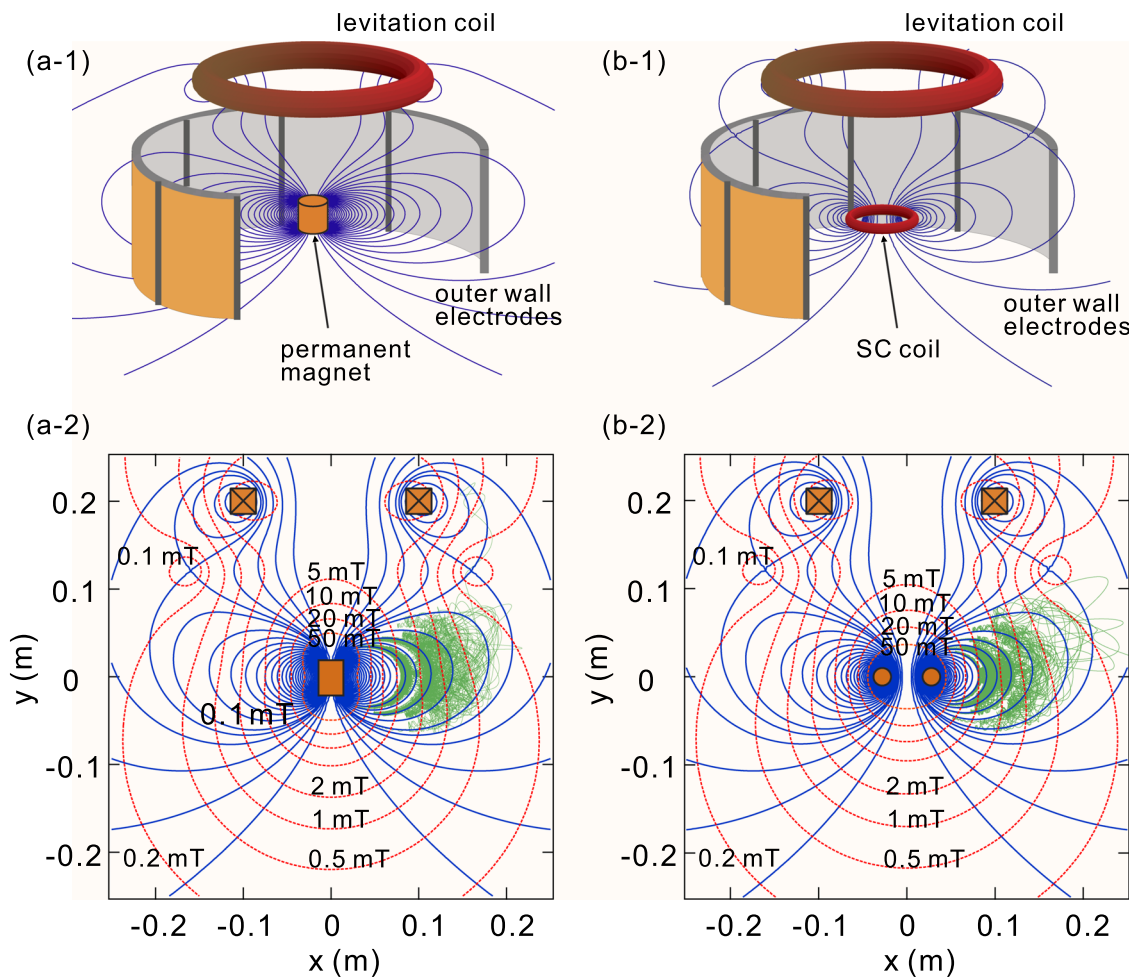

FIG. 14. (1) The schematic views and (2) magnetic configurations of a dipole field trap (a) with a permanent magnet and (b) with a superconducting coil. Green lines (2) show examples of positron orbits projected onto the $r - z$ plane.

those of a permanent magnet, the field lines of a SC coil are closed around the coil, which can greatly reduce the loss of particles compared to the case with a permanent magnet. Here, we compare the trapping properties of dipole field configurations generated by a permanent magnet and a SC coil by numerically calculating the particle orbit in these geometries in order to confirm the expected improvement in confinement in the presence of pitch angle scattering elastic collisions. We assume configurations shown in Fig. 14. When the trap has a levitation coil, the variation of the magnetic fields, especially the appearance of the separatrix, greatly modifies the trapping properties. In order to remove such effects in the comparison and to investigate the variation only caused by the replacement of the permanent magnet with the SC coil, we used levitated trapping geometries for both the permanent magnet and SC coil cases. In Fig. 14(a), a permanent magnet of diameter 28 mm, height 40 mm, and surface field strength $B = 0.6$ T is placed at the equator of the trap. These parameters are the same as those of a magnet used in the prototype APEX experiment.[26] In Fig. 14(b) of the figure, the magnet is replaced with a SC coil with the same magnetic moment, which is generated by a ring current of 9.8 kA and a diameter of 56 mm. The magnet and SC coil are levitated by a pulling force between the lifting coils located in the upward direction, as investigated in Secs. II and III.

In the orbit analysis, we use the parameters of the slow positron beam supplied at the open beam port of NEPOMUC. Specifically, positrons with a parallel kinetic energy of 5 eV with an energy spread of 1 eV and a perpendicular energy spread of 1 eV were injected from positions near the equator of the trap at $r = 8$ cm. The initial positions of the particles were distributed with a full width half maximum of 5 mm. Both the energy spreads and spatial position were given as a randomly sampled Gaussian distribution. Optimization of efficient injection of particles[28] into the SC dipole field trap is beyond the scope of this study although this is an important issue to be studied in future work. The orbit of 1000 particles was calculated with the Bunemann–Boris particle pusher algorithm[46] in the magnetic fields shown in the figure including the effects of neutral collisions. Because the kinetic energy of positrons is quite low, here we considered only random elastic collisions with a constant mean collision frequency ν_{ne}. Due to the variation of guiding the center position caused by the collisions, some particles are lost after being scattered into the loss cone of magnet or onto field lines that intersect the SC coil. We used the surface shape of the magnet as described above and that of the SC coil as a torus with minor radius 10 mm and major radius 28 mm. We also assumed a chamber wall at $r = 250$ mm as another loss channel of positrons. When positrons reached these structures, we judged that they are lost and stopped tracking the orbit in the calculation.

Figure 15 shows the fraction of particles remaining in the trap as a function of time when the mean neutral collision frequency was $\nu_{ne} = 1 \times 10^{-3} f_{gyro}$, where f_{gyro} is the mean cyclotron or gyrofrequency. Here, the fraction of particles at t is defined as the ratio of positrons that are not lost by annihilation on the magnet and coil surfaces or the chamber wall at t after injection at $t = 0$. The typical gyrofrequency of a positron in the trapping region is $f_{gyro} = 1/T_{gyro} = 100$ MHz. Examples of positron orbits [although particle drift toroidally, the orbits shown are projected onto the r–z plane in the right half of each Figs. 14(a-2) and 14(b-2)] clearly show the
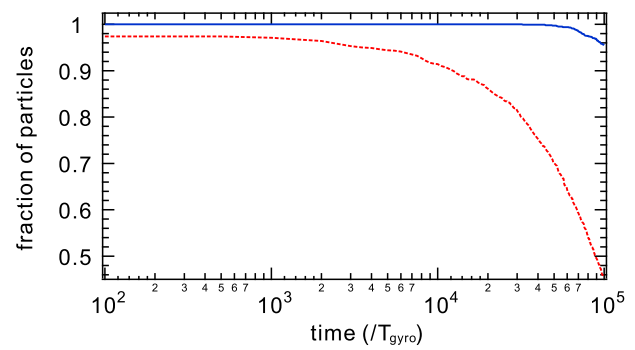

FIG. 15. Fraction of particles remaining in the trap as a function of time in the levitated SC coil (solid line) and permanent magnet (dashed line) configurations when the mean neutral collision frequency is $\nu_{ne} = 1 \times 10^{-3} f_{gyro}$.

variation of the guiding center caused by neutral collisions. In the total calculation time of $10^5 T_{gyro}$, a typical positron makes approximately 100 toroidal rotations due to the curvature and grad-B drift in the dipole magnetic field. In the permanent magnet configuration, as shown by the dashed line in Fig. 15, when particles are initially located in the loss cone, they are promptly lost by hitting the magnet. In the present conditions, the fraction of such positrons was 2.6%. A considerable fraction of positrons are transported into the loss cone and are lost on the magnet surface when neutral collisions affects the positron orbit after $t \sim 1 \times 10^3 T_{gyro}$. In contrast, in the geometry of the SC coil, this loss channel is greatly reduced, as shown by the solid line in the figure. Although there is no loss cone for the SC coil configuration, some of the magnetic field lines intersect the SC coil surface and the chamber wall, as shown in Fig. 14. Because of the radial transport of particles into such regions caused by neutral collisions, positrons are gradually lost after $t \sim 4 \times 10^4 T_{gyro}$ in the present calculation conditions.

For different ν_{ne} values between $10^{-4} f_{gyro}$ and $10^{-2} f_{gyro}$, the fraction of positrons at $t = 10^5 T_{gyro}$ is plotted in Fig. 16. The trapping properties are strongly affected by the neutral collisions. In the permanent magnet trap, where particles are continuously transported into the loss cone, the collision effects are not negligible even at $\nu_{ne} = 10^{-4} f_{gyro}$ (the dashed line in Fig. 16). Most of injected positrons
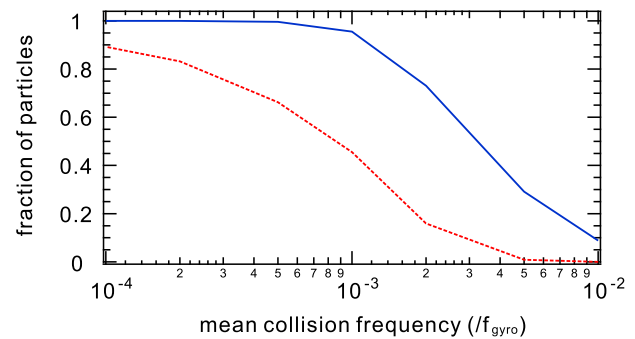

FIG. 16. Fraction of particles at $t = 1 \times 10^5 T_{gyro}$ in a levitated SC coil (solid line) and permanent magnet (dashed line) configurations for various ν_{ne} values.

are lost at $t = 10^5 \, T_{\text{gyro}}$ when ν_{ne} is higher than $5 \times 10^{-3} f_{\text{gyro}}$. By replacing the permanent magnet with the SC coil, as shown by the solid line in Fig. 16, there is a drastic improvement of the trapping properties. While the considerable ratio of particles is lost when $1 \times 10^{-3} < \nu_{\text{ne}}$ because of collisional radial transport toward the SC coil surface and the chamber wall, the fraction of positrons of this new geometry exceeds that of the permanent magnet in the entire ν_{ne} range. Although the ν_{ne} values in the present calculation are not necessarily relevant to the actual experiment due to the calculation time limitation, we can expect the improved confinement properties in the SC dipole compared with the permanent magnet configuration by properly choosing the experimental conditions.

V. CONCLUSION

To conclude, we developed a feedback-controlled magnetic levitation system to be used for the levitation of a superconducting dipole field coil in the APEX pair-plasma project. The properties of the levitation system were investigated using a mock-up experiment with a permanent magnet. Comparison of the experimental results showed fairly good agreement with the numerical analysis of the equilibrium and stability of the magnet motion. These results provide a concrete basis for the design of a compact levitated dipole experiment for the APEX project. Together with the experimental results, in this paper, we also presented a practical review on the levitation physics needed for the construction of a feedback-controlled magnetic levitation system for a charged particle trap. In order to estimate the trapping properties of charged particles in the dipole field trap by replacing the permanent magnet with a levitated superconducting coil, especially to investigate the effects of the reduction in loss cone, we analyzed the orbit of slow positrons in both of the trapping geometries. Assuming a slow radial transport of particles across magnetic field lines, which is realized by collisions with neutral particles in the present study, the comparison calculation showed the possibility of improved confinement properties in the new superconducting dipole field configuration. These results suggest that a levitated superconducting dipole trap is potentially applicable to a compact and low-cost trapping geometry for various charged particles in atomic and non-neutral plasmas, especially for the electron–positron plasmas in the APEX experiment.

REFERENCES

[1] S. Yoshikawa, Nucl. Fusion **13**, 433 (1973).
[2] Z. Yoshida, Y. Ogawa, J. Morikawa, S. Watanabe, Y. Yano, S. Mizumaki, T. Tosaka, Y. Ohtani, A. Hayakawa, and M. Shibui, Plasma Fusion Res. **1**, 008 (2006).
[3] S. M. Krimigis, T. P. Armstrong, W. I. Axford, C. O. Bostrom, C. Y. Fan, G. Gloeckler, L. J. Lanzerotti, E. P. Keath, R. D. Zwickl, J. F. Carbary, and D. C. Hamilton, Science **206**, 977 (1979).
[4] S. M. Mahajan and Z. Yoshida, Phys. Rev. Lett. **81**, 4863 (1998).
[5] Z. Yoshida and S. M. Mahajan, Phys. Rev. Lett. **88**, 095001 (2002).
[6] Z. Yoshida et al., in Proceedings of 17th IAEA Fusion Energy Conference (IAEA), IAEACN-69/ICP/10 (R), 1998.
[7] H. Saitoh, Z. Yoshida, C. Nakashima, H. Himura, J. Morikawa, and M. Fukao, Phys. Rev. Lett. **92**, 255005 (2004).
[8] Y. Ogawa, J. Morikawa, K. Uchijima, Y. Hosaka, C. Kawai, K. Ibano, T. Mito, N. Yanagi, K. Natsume, Y. Terazaki, M. Iwakuma, A. Tomioka, and S. Nose, Plasma Fusion Res. **9**, 1405014 (2014).
[9] Z. Yoshida, H. Saitoh, J. Morikawa, Y. Yano, S. Watanabe, and Y. Ogawa, Phys. Rev. Lett. **104**, 235004 (2010).
[10] M. Nishiura, Y. Kawazura, Z. Yoshida, N. Kenmochi, Y. Yano, H. Saitoh, M. Yamasaki, T. Mushiake, A. Kashyap, and N. Takahashi, Nucl. Fusion **57**, 086038 (2017).
[11] A. Hasegawa, Comments Plasma Phys. Controlled Fusion **11**, 147 (1987).
[12] A. C. Boxer, R. Bergmann, J. L. Ellsworth, D. T. Garnier, J. Kesner, M. E. Mauel, and P. Woskov, Nat. Phys. **6**, 207 (2010).
[13] D. T. Garnier, A. K. Hansen, J. Kesner, M. E. Mauel, P. C. Michael, J. V. Minervini, A. Radovinsky, A. Zhukovsky, A. Boxer, J. L. Ellsworth, I. Karim, and E. E. Ortiz, Fusion Eng. Design **81**, 2371 (2006).
[14] R. C. Davidson, *Physics of Nonneutral Plasmas* (World Scientific, 2001).
[15] J. R. Danielson, D. H. E. Dubin, R. G. Greaves, and C. M. Surko, Rev. Mod. Phys. **87**, 247 (2015).
[16] H. T. Schmidt, R. D. Thomas, M. Gatchell, S. Rosén, P. Reinhed et al., Rev. Sci. Instrum. **84**, 055115 (2013).
[17] Y. Löfgren, Y. Enomoto, T. Masunaga, S. Menk, P. Bertier, and T. Azuma, Rev. Sci. Instrum. **88**, 033110 (2017).
[18] M. Aramaki, Y. Sakawa, and T. Shoji, Jpn. J. Appl. Phys., Part 2 **39**, L246 (2000).
[19] H. Himura, Nucl. Instrum. Methods Phys. Res., Sect. A **811**, 100 (2016).
[20] Z. Yoshida, Y. Ogawa, J. Morikawa, H. Himura, S. Kondoh, C. Nakashima, S. Kakuno, M. Iqbal, F. Volponi, N. Shibayama, and S. Tahara, AIP Conf. Proc. **498**, 397 (1999).
[21] T. Sunn Pedersen and A. H. Boozer, Phys. Rev. Lett. **88**, 205002 (2002).
[22] T. Sunn Pedersen, J. R. Danielson, C. Hugenschmidt, G. Marx, X. Sarasola, F. Schauer, L. Schweikhard, C. M. Surko, and E. Winkler, New J. Phys. **14**, 035010 (2012).
[23] H. Higaki, C. Kaga, K. Fukushima, H. Okamoto, Y. Nagata, Y. Kanai, and Y. Yamazaki, New J. Phys. **19**, 023016 (2017).
[24] H. Chen, F. Fiuza, A. Link, A. Hazi, M. Hill, D. Hoarty, S. James, S. Kerr, D. D. Meyerhofer, J. Myatt, J. Park, Y. Sentoku, and G. J. Williams, Phys. Rev. Lett. **114**, 215001 (2015).
[25] G. Sarri, K. Poder, J. M. Cole, W. Schumaker, A. Di Piazza, B. Reville, T. Dzelzainis, D. Doria, L. A. Gizzi, G. Grittani et al., Nat. Commun. **6**, 6747 (2015).
[26] H. Saitoh, J. Stanja, E. V. Stenson, U. Hergenhahn, H. Niemann, T. S. Pedersen, M. R. Stoneking, C. Piochacz, and C. Hugenschmidt, New J. Phys. **17**, 103038 (2015).
[27] C. Hugenschmidt, C. Piochacz, M. Reiner, and K. Schreckenbach, New J. Phys. **14**, 055027 (2012).
[28] E. V. Stenson, S. Nißl, U. Hergenhahn, J. Horn-Stanja, M. Singer, H. Saitoh, T. Sunn Pedersen, J. R. Danielson, M. R. Stoneking, M. Dickmann, and C. Hugenschmidt, Phys. Rev. Lett. **121**, 235005 (2018).
[29] J. Horn-Stanja, S. Nißl, U. Hergenhahn, T. Sunn Pedersen, H. Saitoh, E. V. Stenson, M. Dickmann, C. Hugenschmidt, M. Singer, M. R. Stoneking, and J. R. Danielson, Phys. Rev. Lett. **121**, 235003 (2018).
[30] J. Stanja, U. Hergenhahn, H. Niemann, N. Paschkowski, T. Sunn Pedersen, H. Saitoh, E. V. Stenson, M. R. Stoneking, C. Hugenschmidt, and C. Piochacz, Nucl. Instrum. Methods Phys. Res., Sect. A **827**, 52 (2016).
[31] J. Horn-Stanja, E. V. Stenson, M. R. Stoneking, M. Singer, U. Hergenhahn, S. Nißl, H. Saitoh, T. S. Pedersen, M. Dickmann, C. Hugenschmidt, and J. R. Danielson, Plasma Res. Exp. **2**, 015006 (2020).
[32] S. Earnshaw, Trans. Cambridge Philos. Soc. **7**, 97 (1842).

[33] V. K. Neil and R. K. Cooper, Rev. Sci. Instrum. **40**, 295 (1969).

[34] C. H. Woods, R. K. Cooper, V. K. Neil, and C. E. Taylor, J. Appl. Phys. **41**, 3295 (1970).

[35] J. File, G. D. Martin, R. G. Mills, and K. E. Wakefield, J. Appl. Phys. **42**, 6 (1971).

[36] I. Echeverra and M. A. Rubio, Rev. Sci. Instrum. **66**, 3931 (1995).

[37] S. Baer, M. A. B. Andrade, C. Esen, J. C. Adamowski, G. Schweiger, and A. Ostendorf, Rev. Sci. Instrum. **82**, 105111 (2011).

[38] J. P. Houlton, M. L. Chen, M. D. Brubaker, K. A. Bertness, and C. T. Rogers, Rev. Sci. Instrum. **89**, 125107 (2018).

[39] J. Morikawa, D. Ozawa, Y. Ogawa, N. Yanagi, S. Hamaguchi, and T. Mito, Jpn. J. Appl. Phys., Part 2 **40**, L1029 (2001).

[40] N. Yanagi, J. Morikawa, T. Mito, Y. Ogawa, S. Hamaguchi, H. Chikaraishi, M. Iwakuma, T. Uede, I. Itoh, S. Nose, and S. Fukui, IEEE Trans. Appl. Supercond. **12**, 948 (2002).

[41] Y. Ogawa, J. Morikawa, K. Ohkuni, H. Nihei, D. Hori, S. Yamakoshi, T. Goto, T. Mito, N. Yanagi, M. Iwakuma, and T. Uede, Teion Kogaku, J. Cryog. Soc. Jpn. **39**, 175 (2004) (in Japanese).

[42] J. Morikawa, K. Ohkuni, D. Hori, S. Yamakoshi, T. Goto, Y. Ogawa, N. Yanagi, and T. Mito, Teion Kogaku, J. Cryog. Soc. Jpn. **39**, 209 (2004) (in Japanese).

[43] Y. Yano, Z. Yoshida, Y. Ogawa, J. Morikawa, and H. Saitoh, Fusion Eng. Des. **85**, 641 (2010).

[44] M. R. Stoneking, H. Saitoh, M. Singer, E. V. Stenson, J. Horn-Stanja, S. Sunn Pedersen, S. Nißl, U. Hergenhahn, N. Yanagi, C. Hugenschmidt, M. Dickmann, J. R. Danielson, and C. M. Surko, AIP Conf. Proc. **1928**, 020015 (2018).

[45] A. Hurwitz, Math. Ann. **46**, 273 (1895).

[46] H. Qin, S. Zhang, J. Xiao, J. Liu, Y. Sun, and W. M. Tang, Phys. Plasmas **20**, 084503 (2013).